

Unfolding slow muon depth profiles with universal range distributions

Eduardo F M Ribeiro¹, Rui C Vilão¹, Helena V Alberto¹, João M Gil¹ and Alois Weidinger²

¹CFisUC, Department of Physics University of Coimbra R. Larga, Coimbra P-3004-516, Portugal

²Department ASPIN Helmholtz-Zentrum Berlin für Materialien und Energie 14109 Berlin, Germany

E-mail: lena@uc.pt

Abstract. The analysis of depth-dependent data of thin film semiconductor heterostructures is discussed in this work. The data is obtained by varying muon implantation energy, E , using the Low-Energy Muon (LEM) facility at PSI, Switzerland. Since the measurement method has a finite resolution, unfolding of the measured profile with the resolution function is required. The unfolding can be performed in the real space (that is in depth variable x), using range distribution function, $P(x, E)$, obtained by Monte Carlo simulations. As will be shown, it is much simpler to perform the unfolding in the implantation energy space and to transform the results afterwards into real space. This simplifies the analysis considerably, since the universal range distributions can be used, independent of the specific sample.

1. Introduction

The development of slow-muon beamlines [1, 2] has allowed the investigation of nanometer size heterostructures [3]. In thin-film photovoltaic devices, effects at the interface are known to play an important role in its functioning and efficiency, which is often not fully understood [4, 5, 6]. A local-probe method such as μ SR may therefore bring important microscopic information not available by other techniques [7, 8, 9].

However, the analysis of the μ SR data obtained using implantation with slow muons in a typical range of 3 keV to 25 keV is affected by finite depth-resolution due to range straggling. The range distributions depend on the density of the material and on the atomic number of the sample constituents. The range profiles may extend over several tens of nanometers, causing an overlap of muons stopping in different layers, which complicates the analysis additionally. In this paper we will present in detail a new method to overcome this difficulties which was applied already in [9] but was not discussed in detail yet.

In the examples analysed in this work, the time spectra are simple diamagnetic oscillations (Fig. 1), fitted with one gaussian-damped cosine function given by

$$A(t) = A_{\text{dia}} \exp\left(-\frac{1}{2}\sigma^2 t^2\right) \cos(\omega t + \phi) \quad (1)$$

The experimental diamagnetic asymmetry A_{dia} thus obtained gives the corresponding fraction f_{dia} of muons stopping in a diamagnetic configuration, upon comparison with a calibration using



silver. For thin-film semiconductor heterostructures, the dependence of the diamagnetic fraction as a function of the implantation energy, E , is often the main experimental result.

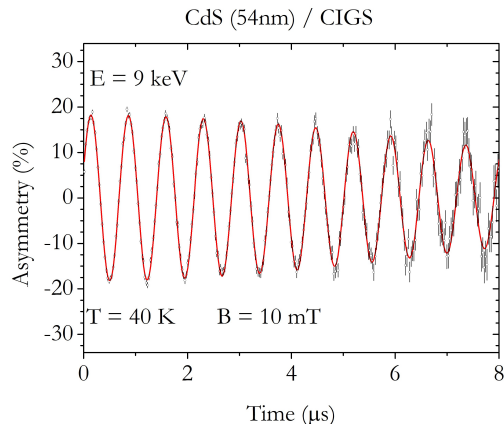


Figure 1. Typical μ SR time spectrum for a CdS(54 nm)/CIGS sample (implantation energy $E = 9$ keV). The measurement was performed at the Low-Energy Muon (LEM) Instrument at $T = 40$ K in transverse field of $B = 10$ mT. The line is a one-component fit with a Gaussian-damped cosine function.

2. Unfolding procedure

The unfolding (or deconvolution) is performed by convoluting a trial function with the resolution function of the measurement and fit it to the experimental data. The optimum fit gives the unfolded depth profile of the diamagnetic fraction

2.1. Unfolding in depth space

The experimental diamagnetic fraction at implantation energy E , $f_{\text{dia}}^{\text{exp}}(E)$, corresponds to the convolution of the real diamagnetic fraction at depth x , $f_{\text{dia}}(x)$, with the (normalized) range distribution function $P(x, E)$ calculated using the TRIM.SP software [11, 1]:

$$f_{\text{dia}}^{\text{exp}}(E) = \int_0^{\infty} P(x, E) f_{\text{dia}}(x) dx. \quad (2)$$

For multilayer systems, the range distribution depends on the width of the different layers and on the atomic composition and density of each layer. Fig. 2 shows the calculated range distributions at 8 keV for different materials. A large variation is observed in both the average range and the width of the distributions. For multilayer systems, the distributions become even more complex, especially in the interface region between different layers. Calculating $P(x, E)$ for multilayered systems requires a previous knowledge of the widths of the different layers, which is not always known with enough precision.

2.2. Unfolding in energy space

It seems natural to perform the unfolding directly on the measured depth profiles, since the underlying structure of the profile can be guessed directly from the measured data. The structure of the profile is washed out because not all muons stop at the same depth, some below, some above the average range. Thus, there is again a range distribution, but now measured in energy. The distribution $P(E', E)$ is used in the convolution procedure:

$$f_{\text{dia}}^{\text{exp}}(E) = \int_0^{\infty} P(E', E) f_{\text{dia}}(E') dE'. \quad (3)$$

$P(E', E)$ is obtained from $P(x, E)$ by a coordinate transformation. This requires scaling from the x -scale to the E' -scale via a relation $x = f(E')$. The conversion between the two distributions is obtained via

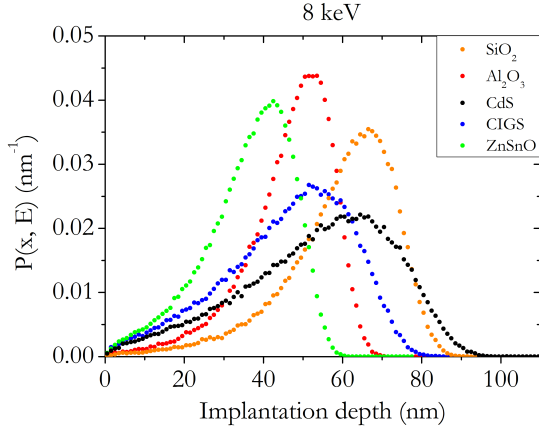


Figure 2. Range distributions as a function of depth, for an implantation energy of 8 keV, normalized to the muons stopping in the sample, for some selected materials: SiO₂, CdS, CIGS, Al₂O₃ and ZnSnO.

$$P(E', E) dE' = P(x, E) dx = P(x, E) \frac{dx}{dE'} dE'. \quad (4)$$

We use for the scaling the relation between the median of the range distribution and the implantation energy E (see Fig. 3). This ensures that the resulting range distributions in energy space are centered at the implantation energy E . One could also use the average range versus E for this transformation, but this does not guarantee that the distributions are centered on E .

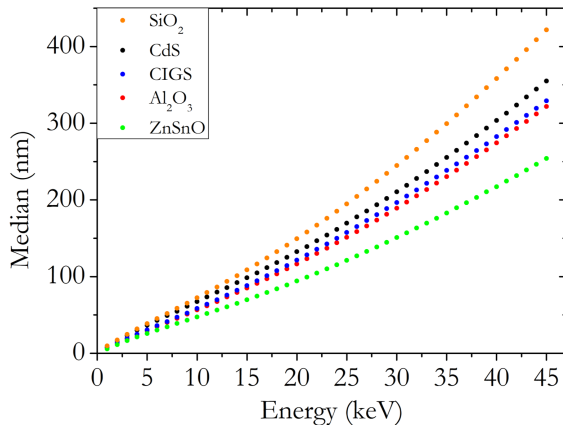


Figure 3. Median depth of the range distribution, for several materials, as a function of implantation energy. The assumed compositions and densities are: Cu_{0.87}In_{0.61}Ga_{0.39}Se₂ ($\rho = 5.70$ g/cm³), CdS ($\rho = 4.80$ g/cm³), Zn_{0.82}Sn_{0.18}O_{1.1} ($\rho = 5.3$ g/cm³), Al_{0.45}O_{0.55} ($\rho = 3.0$ g/cm³), Si_{0.37}O_{0.63} ($\rho = 2.2$ g/cm³).

Figure 4 shows the range distributions in energy space for implantation energy of 8 keV for different materials. They are all centered at 8 keV, but the widths are different. Two main groups can be identified, those corresponding to high atomic numbers of the constituents (CIGS, ZnSnO and CdS) and those with lower atomic numbers (Al₂O₃ and SiO₂), the latter showing narrower curves. However, as will be discussed below, these differences have only a minor effect on the final results.

3. The universal range distributions

Figure 5 shows representative range distributions $P(E', E)$ for implantation energies between 3 keV and 28 keV. They are calculated for CdS with the scaling from the median in x-space to energy, but are considered applicable for all samples. As discussed above they are only approximate since the widths of the range distributions of different samples may be different. But this difference affects only the slope at the transition between different layers and has

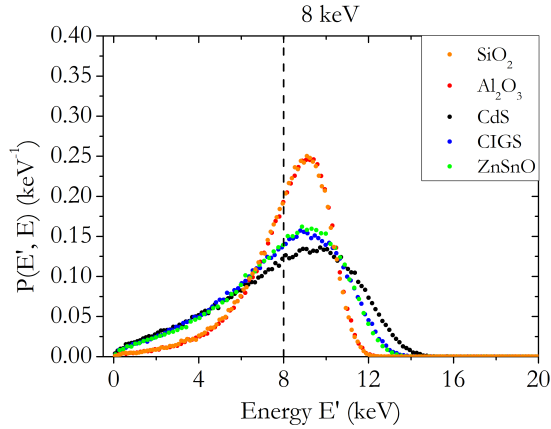


Figure 4. Normalized near-universal range distribution functions $P(E', E)$ in energy space (Eq. 4), for the same materials shown in Fig. 3, for an implantation energy $E = 8$ keV.

usually no large influence on the extracted results. One may also consider to use a second set of distributions derived e.g. from Al_2O_3 , and use them in case of samples with lighter elements.

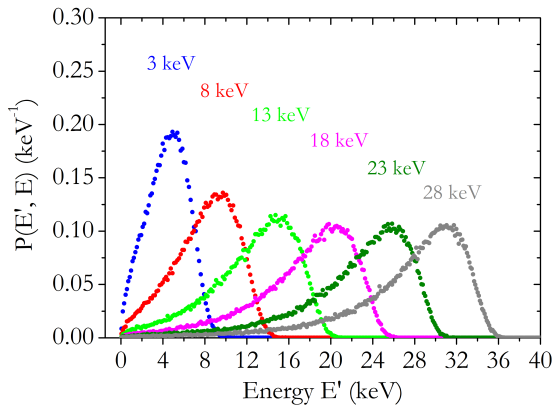


Figure 5. Normalized universal range distributions $P(E', E)$ (Eq. 4) for different implantation energies. They are derived for CdS but are approximately applicable also for other samples.

4. Example CdS/CIGS and comparison of the different methods

The aim of the slow-muon experiments is to arrive at the real profile $f_{\text{dia}}(x)$ in the depth space or, correspondingly, at the real profile $f_{\text{dia}}(E')$ in the energy space. In order to proceed to the deconvolution, a simple model for $f_{\text{dia}}(x)$ has been assumed in [7, 10, 8], and we now take a similar model for $f_{\text{dia}}(E)$. Representative data for a CdS/CIGS interface have been selected for this demonstration, where the CdS buffer layer has a nominal width of 54 nm. The experimental data $f_{\text{dia}}^{\text{exp}}(E)$ are shown in Fig. 6 (a) and (b). As described elsewhere [9], the data analysis requires three distinct space regions, corresponding to the buffer layer (CdS), to an extended defect region in CIGS (close to the CdS/CIGS interface), and to bulk CIGS. The simple model applied has five parameters, corresponding to the diamagnetic fraction in each region (f_1 , f_2 and f_3 , respectively) and to the depth of the corresponding borders, expressed either in the real space (x_1 and x_2) or in the energy space (E_1 and E_2). These five parameters are used to fit the experimental data $f_{\text{dia}}^{\text{exp}}(E)$, using either eq. 2 or eq. 3. The corresponding fitting curves are shown as well in Fig. 6 (a) and (b). The fitted parameters of the respective models for $f_{\text{dia}}(x)$ and $f_{\text{dia}}(E)$ are shown in Fig. 6 (c) and (d). We recall that the analysis in the depth space (Fig. 6 (a) and (c)) relies on $P(x, E)$ curves from Monte-Carlo simulations assuming a given width for the CdS layer (in this case, 59 nm was assumed). For the analysis in the energy

space, the CdS $P(E', E)$ distribution provides a natural choice for the analysis of a CdS/CIGS heterostructure.

However, in order to show the near-universality of the different $P(E', E)$ distributions, we show in Fig. 6 (b) and (d) the analysis of the same CdS/CIGS data using the $P(E', E)$ distributions for CdS (black lines) and Al_2O_3 (red lines), which correspond to materials with very different densities.

The results of the fits shown in Fig. 6 are shown in Table 1, which clearly demonstrates that any of the methods give consistent results within the uncertainties.

The comparison of the fit in the energy space (using the CdS $P(E', E)$ distribution) with that in the depth space shows not only the equivalence of the fit quality, but also the intuitive character of the fit in the energy space. Moreover, fitting in the energy space does not require *a priori* knowledge of the width of the CdS layer. The comparison of the fits in Fig. 6 (b) and (d), using very different materials, strongly suggest a "near-universality" of $P(E', E)$ distributions.

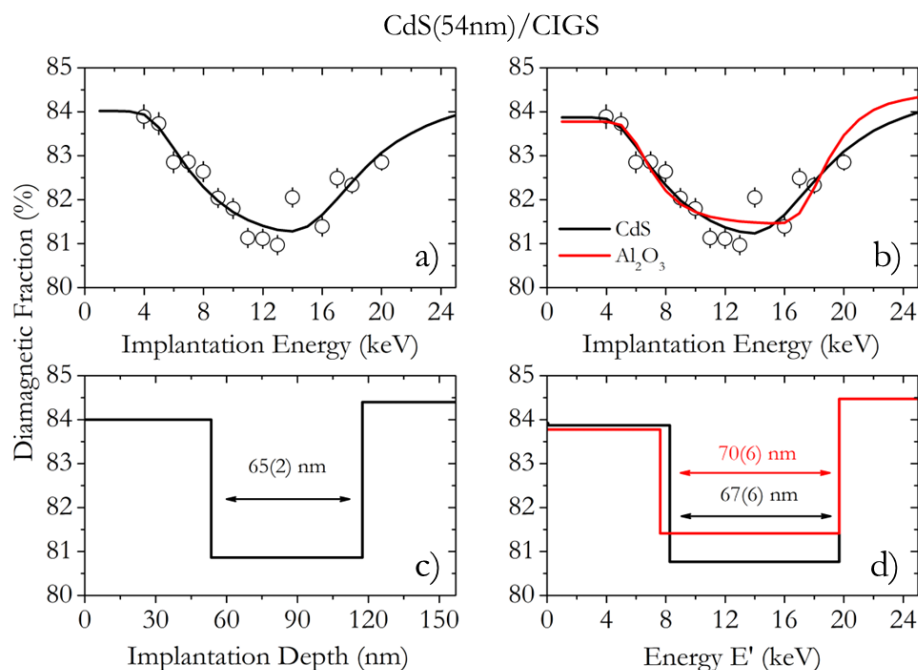


Figure 6. Analysis of slow muon implantation profiles of a CdS/CIGS heterostructure, with a nominal width of 54 nm of the CdS buffer layer, using different methods. a) and c): analysis in the depth space, as in Ref.[7]. b) and d): analysis in the energy space, using the $P(E', E)$ for CdS (black) and Al_2O_3 (red). The top frames a) and b) show the experimental data as well as the fit lines to eq. 2 or eq. 3; the bottom frames show the fitted parameters of the assumed model for the profiles $f_{dia}(x)$ and $f_{dia}(E')$.

5. Conclusions

A novel method for performing the unfolding of the depth profiles of slow-muon data in semiconductor heterostructures was presented. The advantages of doing the analysis in the energy space instead of the depth space were discussed, based on the comparison of different approaches in the analysis of a common dataset of a CdS/CIGS heterostructure. The near-universal character of the corresponding distributions in the energy space was discussed. This

Table 1. Values of the parameters obtained in the fits with different unfolding procedures: $P(x, E)$ the distributions in real space and $P(E', E)$ the distributions in energy space derived from CdS and Al_2O_3 , respectively. The parameters f_1 and f_2 are the diamagnetic fractions in the bulk and in the dip, E_1 and E_2 the energies at the transitions between regions, and x_1 and $x_2 - x_1$ the thicknesses of the top and the dip layer, respectively.

	$P(x, E)$ (CdS/CIGS)	$P(E', E)$ (CdS)	$P(E', E)$ (Al_2O_3)
f_1 (%)	84	83.9(2)	83.7(1)
f_2 (%)	80.9(1)	80.8(1)	81.4(1)
E_1 (keV)	—	8.21(6)	7.66(8)
E_2 (keV)	—	19.7(4)	19.7(1)
x_1 (nm)	53.1(4)	56(1)	53(1)
$x_2 - x_1$ (nm)	65(2)	67(6)	70(7)

method opens the way to a simpler analysis approach to low-energy μSR data in thin-film heterostructures.

Acknowledgments

This work is based on experiments performed at the Swiss Muon Source ($S\mu\text{S}$), Paul Scherrer Institute, Villigen, Switzerland and was supported with funds from FEDER (Programa Operacional Factores de Competitividade COMPETE) and by national funds from FCT - Fundação para a Ciência e Tecnologia, I. P. (Portugal) under projects PTDC/FIS-MAC/29696/2017, UID/04564/2020.

References

- [1] Morenzoni E, Glückler E H, Prokscha T, Khasanov R, Luetkens H, Birke M, Forgan E M, Niedermayer Ch, Pleines M 2002, Implantation studies of keV positive muons in thin metallic layers, *Nucl. Instrum. Methods Phys. Res. B: Beam Interactions with Materials and Atoms* **192**, 254.
- [2] Prokscha T Morenzoni E, Deiters K, Foroughi F, George D, Kobler R, Suter A, Vrankovic V 2008, The new beam at PSI: a hybrid-type large acceptance channel for the generation of a high intensity surface-muon beam, *Nucl. Instrum. Methods Phys. Res. A* **595**, 317.
- [3] Hillier, A D , Blundell, S J, McKenzie, I et al. 2022, Muon spin spectroscopy, *Nat Rev Methods Primers* **2**, 4.
- [4] Allen T G, Bullock J, Yang X, Javey A and De Wolf S 2019 *Passivating contacts for crystalline silicon solar cells*, *Nature Energy* **4**, 914.
- [5] Curado M A et al 2020, Front passivation of $\text{Cu}(\text{In,Ga})\text{Se}_2$ solar cells using Al_2O_3 : culprits and benefits, *Applied Materials Today* **21**, 100867.
- [6] Cunha J M V et al. 2018, Insulator materials for interface passivation of $\text{Cu}(\text{In,Ga})\text{Se}_2$ thin films, *IEEE Journal of Photovoltaics* **8**, 1313.
- [7] Alberto H V et al 2018, Slow-muon study of quaternary solar-cell materials: single layers and p-n junctions, *Physical Review Materials* **2** 025402.
- [8] Ribeiro E, Alberto H V, Vilão R C, Gil J M, Weidinger A, Salomé P M P, Prokscha T, Suter A, and Salman Z, 2020, CdS versus ZnSnO buffer layers for a CIGS solar cell: a depth-resolved analysis using the muon probe, *EPJ Web of Conferences* **233**, 05004.
- [9] Alberto H V et al 2022, Characterization of the interfacial defect layer in chalcopyrite solar cells by depth-resolved muon spin spectroscopy, *Adv. Mater. Interfaces*, 2200374
- [10] Simões A F A, Alberto H V, Vilão R C, Gil J M, Cunha J M V, Curado M A, P. Salomé P M P, Prokscha T, Suter A, and Salman Z 2020, Muon implantation experiments in films: obtaining depth-resolved information, *Rev. Sci. Instrum.* **91**, 023906.
- [11] Eckstein W, 1991 *Computer Simulations of Ion-Solid Interactions* (Springer, Berlin, Heidelberg, New York)